

Polariton Creation in Coupled Cavity Arrays with Spectrally Disordered Emitters

Jesse Patton,^{1,*} Victoria A. Norman,^{1,2,*} Richard T. Scalettar,² and Marina Radulaski^{1,†}

¹*Department of Electrical and Computer Engineering,
University of California, Davis, CA 95616, USA*

²*Department of Physics, University of California, Davis, CA 95616, USA*

(Dated: May 2, 2023)

Integrated photonics has been a promising platform for analog quantum simulation of condensed matter phenomena in strongly correlated systems. To that end, we explore the implementation of all-photonic quantum simulators in coupled cavity arrays with integrated ensembles of spectrally disordered emitters. Our model is reflective of color center ensembles integrated into photonic crystal cavity arrays. Using the Quantum Master Equation and the Effective Hamiltonian approaches, we study energy band formation and wavefunction properties in the open quantum Tavis-Cummings-Hubbard framework. We find conditions for polariton creation and (de)localization under spectral disorder and for variable ratios of emitter-cavity and cavity-cavity interactions. To quantify these properties, we introduce two metrics, the polaritonic and the nodal participation ratio, that characterize the light-matter hybridization and the node delocalization of the wavefunction, respectively. These new metrics combined with the effective Hamiltonian approach prove to be a powerful toolbox for cavity quantum electrodynamical engineering of solid-state systems.

I. INTRODUCTION

Quantum simulation has attracted scientific attention since the early 1980s ignited by Richard Feynman’s vision of the necessity of quantum mechanics in the modeling of natural phenomena [1]. Proposed implementations have included atomic, trapped ion, superconducting and photonic platforms [2–7]. Here we focus on solid-state optical systems due to their potential for growth into large-scale commercial quantum simulators [8–11].

Nanophotonic cavities integrating quantum emitters have served as a rich playground for exploring quantum optics phenomena in solid-state systems. This includes demonstrations of weak [12] and strong [13] cavity quantum electrodynamical (QED) coupling, photon blockade and photon-induced tunneling [14], ultra-fast modulation of optical signals [15], and more. The large dipole moment of quantum emitters, paired with (sub)wavelength scale optical mode volumes in photonic crystal cavities, give rise to high optical nonlinearities and light-matter state hybridization that creates polaritons. Polaritonic interactions in nanophotonic systems can be several orders of magnitude higher than those achieved in atomic systems. Such strong interaction has been at the core of theoretical proposals for quantum state transfer [16, 17], as well as for the photonic simulation [18, 19] of Bose-Hubbard and fractional quantum Hall physics. Here, the system is made of an array of coupled cavities, each in the strong coupling regime of cavity QED, and described by the Jaynes-Cummings-Hubbard model. However, this model has been experimentally hard to achieve.

While the progress toward the realization of coupled cavity arrays (CCAs) with embedded emitters has been

made with quantum dots [20, 21], the spectral disorder of these emitters has been a major roadblock to developing a large-scale resonant system. This problem is not present to such a significant extent with color center emitters, which are atomic defects in wide band gap materials. Recently, color center integration with nanocavities in diamond [22, 23] and silicon carbide [24, 25] has been demonstrated in the weak cavity QED coupling regime. Though this regime is unsuitable for studies of polaritonic physics, proposals to demonstrate strong cavity QED regime have been presented with cavities integrating several (M) emitters, as opposed to a single emitter. Additionally, there has been renewed interest in disordered cavity QED systems with the discovery of phenomena like collectively induced transparency [26]. Such systems are described by the Tavis-Cummings, rather than the Jaynes-Cummings model. Here, the collective coupling of emitters to the cavity effectively boosts the light-matter interaction rate by a factor of \sqrt{M} . Due to the small, but nonzero, spectral disorder of color centers, the collective strong coupling is possible within the *cavity protection* regime, if its rate overcomes the spectral disorder Δ of color centers [27, 28], i.e. $\Delta < g\sqrt{M}$. Such disordered multi-emitter cavity systems have been explored for applications in quantum light generation [29–31].

Here, we explore how all-photonic quantum simulators based on coupled cavity arrays can benefit from an increased interaction rate established in multi-emitter cavity QED. We expand the Jaynes-Cummings-Hubbard approach to the *spectrally disordered* Tavis-Cummings-Hubbard model (TCHM) [32] and define conditions for polariton creation utilized in all-photonic quantum simulation, aided by the introduction of new localization metrics inspired by condensed matter approaches. Our model targets applications in technologically mature solid-state platforms and is reflective of the state-of-the-art parameters achieved in silicon carbide and diamond color center hosts.

* equal contribution

† mradulaski@ucdavis.edu

II. THE CCA QED MODEL

Our CCA QED model captures the single-excitation regime of the spectrally disordered Tavis-Cummings-Hubbard model comprised of emitter-cavity localizing interactions and cavity-cavity delocalizing interactions:

$$H_{\text{TCHM}} = \sum_{n=1}^N \left\{ \omega_{c,n} a_n^\dagger a_n + \sum_{m=1}^{M_n} \left[\omega_{e,n,m} \sigma_{n,m}^+ \sigma_{n,m}^- + g_{n,m} (a_n^\dagger \sigma_{n,m}^- + \sigma_{n,m}^+ a_n) \right] - J_{n,n+1} (a_n^\dagger a_{n+1} + a_{n+1}^\dagger a_n) \right\}, \quad (1)$$

where N is the number of cavities in the array, M_n is the number of emitters in the n -th cavity, $\omega_{c,n}$ and a_n represent the angular frequency and the annihilation operator of the n -th cavity, $\omega_{e,n,m}$, $\sigma_{n,m}^-$ and $g_{n,m}$ correspond to the angular frequency, the lowering operator and the emitter-cavity coupling rate of the m -th emitter in the n -th cavity, $J_{n,n+1}$ is the photon hopping rate between the enumerated neighboring cavities. In this work we will assume $\omega_{c,n} = \omega_c$, $g_{n,m} = g$ and $J_{n,n+1} = J$.

A. Non-disordered CCA QED model

Before examining the spectral disorder effects in CCA QED, let us first address the energy spectrum in the fully resonant system of a linear array of coupled cavities with identical emitters. Here, the eigenenergy spectrum features two CCA polariton bands with N states, each, and a degenerate set of $N(M + 1)$ subradiant states as illustrated in Figure 1. The polariton band states are parameterized by discrete momenta $k = k_p = \pi p / (N + 1)$, ($p = 1, 2, 3, \dots, N$) as

$$E(k) = \omega_c - J \cos k \pm \sqrt{J^2 \cos^2 k + Mg^2}. \quad (2)$$

The origin of these spectral features can be decomposed to the QED and the CCA components. The resonant Tavis-Cummings model of M emitters in $N = 1$ cavity has the spectrum of two polaritons and $M - 1$ degenerate subradiant states, while a CCA of $N > 1$, $M = 0$ cavities has a single spectral band of N photonic states. The spectrum of the resonant Tavis-Cummings-Hubbard model is a product of these components. This system has close analogs to the condensed matter models it aims to simulate.

B. The Condensed Matter analogs

For cavity-emitter arrays with translationally invariant energy scales ($\omega_{c,n} = \omega_c$, $\omega_{e,n,m} = \omega_e$, $g_{n,m} = g$,

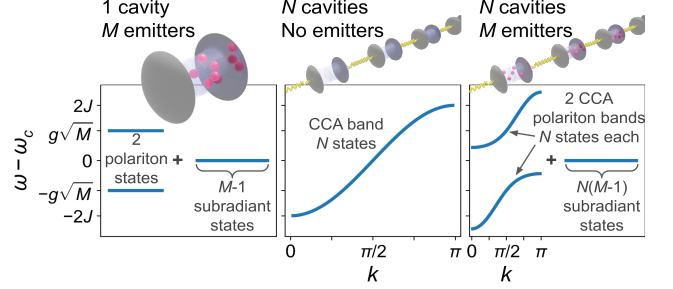


FIG. 1. The eigenspectra of non-disordered coupled cavity arrays with open boundary conditions. (Left) One cavity with M emitters has two polariton states and $M - 1$ subradiant states. (Middle) CCA of N cavities with no emitters has one CCA band of N states. (Right) CCA of N cavities and M emitters per cavity has two polariton bands, upper and lower, of N states each and $N(M - 1)$ subradiant states.

$J_{n,n+1} = J$), one can solve for the eigenvalues and eigenvectors analytically, both for open and periodic ($a_1 \equiv a_{N+1}$) boundary conditions. Indeed, much of the derivation precisely parallels the calculation of the band structure of tight binding Hamiltonians commonly studied in condensed matter physics, as detailed in the Appendix. The case of no emitters ($M_n = 0$) corresponds to the $d = 1$ (Bose) Hubbard Model (HM), and the case with a single emitter in each cavity ($M_n = 1$) to the Periodic Anderson Model (PAM), though analogs between the single emitter per cavity systems and the HM have also been drawn [33]. We should note that in the latter part of the study we will use open boundary condition due to its correspondence to experiment.

Indeed, there are a number of connections between the Tavis-Cummings-Hubbard model (TCHM), considered here in the context of CCAs, and the various Hamiltonians which are used to model strongly correlated fermion materials in condensed matter physics. For one emitter per cavity, our model has an identical geometry to the Periodic Anderson Model (PAM): the hopping of photons between cavities is analogous to the conduction electrons which hybridize between different sites, and the photon-emitter coupling maps onto the hopping between the conduction electrons and localized orbitals which, like the emitters, do not have a direct intersite (intercavity) overlap. Thus, in the single excitation sector, and for one emitter per cavity, the models are *identical*.

However, there are significant limitations to this analogy: If the number of excitations is greater than one, the bosonic nature of the photons in the CCA problem introduces a fundamental difference between the TCHM and the PAM. Further, the fermions in the PAM have a spin index, so there are two species of these particles. As long as the local Coulomb repulsion $U = 0$ in the PAM, these two species are independent and hence can be considered as two independent copies of the TCHM. However this breaks down for $U \neq 0$ and multiple excitations. Finally, the PAM does not admit multiple localized modes on dif-

ferent sites, so it only maps to the case of a single emitter per cavity.

It is worth noting, however, that the CM community has considered many variants of models which mix localized and itinerant quantum particles: the Kondo lattice model (KLM) replaces the two spin species of the localized electrons on each site by a single spin, thereby *reducing* the number of local degrees of freedom per site to two, the same value as an emitter in the TCHM. On the other hand, in the *large- N limit* the number of local degrees of freedom is *expanded*. Crudely speaking, these variants are similar to adjusting the number of emitters per cavity.

Thus, while it defies a specific mapping onto a condensed matter Hamiltonian, the TCHM provides another, novel and interesting, way of exploring the interplay of itinerant and mobile quantum particles. It is *distinct* from the condensed matter models, but we believe that a careful exploration of its properties, as provided in our manuscript, holds lessons for the CM model Hamiltonian community, especially in view of the many variants of models already in play there. As one example, the *polaritonicity* (degree of light-matter hybridization) upon which we focus in the sections to follow, holds lessons for *singlet formation* in which local and itinerant electrons become tightly intertwined in the PAM and KLM.

III. EFFECTS OF SPECTRAL DISORDER ON POLARITON FORMATION

A. Model parameters

The parameters of our model have been selected as representative of silicon carbide and diamond color center platforms. Recent demonstrations of emitter-cavity interaction in photonic crystal cavities support rates of approximately $g/2\pi \sim 2\text{-}7.3$ GHz [24, 34], therefore, we chose a constant value of $g/2\pi = 5$ GHz. While a variation in the coupling rate g among emitters is likely to occur due to their variable positioning inside the electromagnetic mode, our prior work indicates that the collective emitter-cavity coupling still takes place [27] at a well defined rate of $g_M = \sqrt{\sum_{m=1}^M g_m^2}$. Therefore, keeping g constant among the emitters should not take away from the overall phenomenology studied here.

The experimentally demonstrated cavity loss rates reach as low as $\kappa/2\pi \sim 15\text{-}50$ GHz [24, 34], while recent modeled designs could reduce these values by at least an order of magnitude [35]. With a slight optimism, we chose cavity loss rate of $\kappa/2\pi = 10$ GHz. Our recent designs of photonic crystal molecules indicate that coupled cavity hopping rates can be straightforwardly designed in the range $1\text{ GHz} < J/2\pi < 200\text{ GHz}$ [35], thus spanning systems from the dominant cavity QED to the dominant photonic interaction character, represented in our choice of values $J/g = 0.1, 1, 10$.

Fabrication imperfections may yield drifts in cavity resonant frequencies and hopping rates. The effect of this issue was studied in another platform where GaAs coupled cavity arrays were integrated with quantum dots [21] and indicates that the coupling strength is an order of magnitude higher than the frequency and hopping rate perturbations. We apply this assumption in our model, maintaining that all cavities are mutually resonant and all rates J are constant.

The spectral inhomogeneity of emitters in fabricated devices, the main study of our model, has been characterized as $\Delta \sim 10$ GHz for a variety of emitters in silicon carbide and diamond [36, 37]. We represent this parameter through its relation to the collective coupling rate $g\sqrt{M}$ in a cavity, spanning the spectral inhomogeneity across a range of values. It is worth noting that the vibronic resonances are two orders of magnitude larger than the inhomogeneous broadening, for example 8.7 THz for the silicon vacancy in 4H-SiC [38, 39], therefore the phonon side band is not expected to play a part in the collective emitter-cavity coupling process. Emitter lifetime in color centers is usually in the 1-15 ns range [40], we select the value $\gamma/2\pi = 1/5.8$ GHz as representative. Due to γ being the lowest rate in the system, its minimal variations among emitters [37] affect the system only marginally, therefore we assume it has a constant value in the system. Lifetime- and nearly lifetime-limited emission of color centers has been demonstrated upon photonic integration [37, 41, 42]. Due to this experimental advance, our model does not consider the dephasing terms, though such analysis may prove valuable with further development of integrated coupled cavity arrays.

B. Polariton Characteristics in small TCHM systems

We present results for the $N = 2, M = 2$ system using three closely related approaches to TCHM systems. The Quantum master equation (QME) solves the Lindbladian master equation exactly in the low-excitation regime [43]. The effective Hamiltonian (H_{EFF}) uses the established non-hermitian effective approach to modeling Hamiltonians that are too resource intensive for the current state of the art classical computers to solve. Its approximation effectiveness is limited to the single-excitation regime, which is suitable for our exploration. The final characterization is one we introduce in this paper, the nodal and polaritonic participation ratios (P_N and P_P , respectively). This method is derived from the condensed matter participation ratio metrics [44] used to quantify a system's localization properties. The P_N and P_P metrics are applied to eigenstates of the H_{EFF} to quantify the delocalization and light-matter hybridization of the wavefunction, respectively. The spectral disorder is implemented by sampling emitter angular frequency, ω_e , from a Gaussian distribution $P(\omega_e) = \frac{1}{\sqrt{2\pi}\sigma} \exp\left\{-\frac{(\omega_e - \omega_c)^2}{2\sigma^2}\right\}$ centered at ω_c with a width of $\Delta = 2\sigma$.

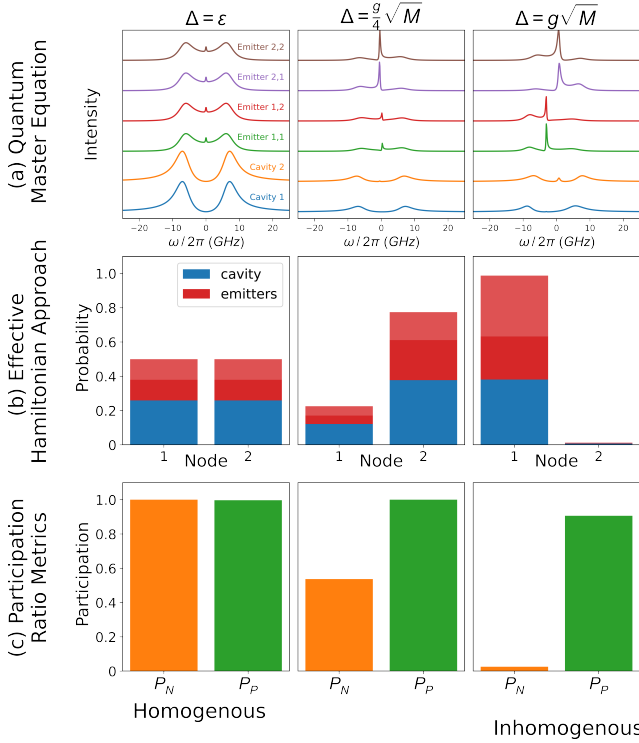


FIG. 2. Representative plots calculated for the disordered $N = 2, M = 2$ TCHM for all three approaches. The parameters of the system are $g/2\pi = 5$ GHz, $J/g = 0.1$, $\kappa/2\pi = 10$ GHz, $\gamma/2\pi = 1/5.8$ GHz, $\omega_c = 0$, $\omega_e = \omega_c + \Delta$. The spectral disorder Δ is indicated above the plot columns ($\epsilon \approx 0$). All three approaches used the identical values of ω_e sampled from a Gaussian distribution of width Δ (single random realization for each Δ) for direct comparison. Emitters 1,1 and 1,2 are in Cavity 1 (Node 1) and Emitters 2,1 and 2,2 are in Cavity 2 (Node 2). In (a) the low-power pulse-excitation of the Cavity 1 is $P = 0.01$. Spectral intensity is essentially a measure of how likely it is for an emitted photon to have a particular frequency. The bright central peaks that appear for the non-vanishing disorder are the subradiant states. The node occupancy (b) and the participation ratios (c) for the lowest energy eigenstate. The shades of red represent wavefunction components of different emitters in the same node (cavity with emitters), while the blue represents the cavity component.

In the small system that is solvable exactly using the QME approach, we test parameters that take a resonant Tavis-Cummings-Hubbard model from two nearly isolated Tavis-Cummings models ($J/g = 0.1$), to a system with delocalized polaritons ($J/g = 1$), and all the way to a photonic molecule loosely coupled to emitters ($J/g = 10$). While we present only the $J/g = 0.1$ results here, corresponding to the least cavity-cavity interaction, the results of the other cases are available in the Appendix.

1. The Quantum Master Equation Approach

For the exact solution of the open quantum system Tavis-Cummings-Hubbard model, we have developed a software package [45] that solves the Quantum Master Equation (QME). Our code uses the Quantum Toolbox in Python (QuTiP) [46] which solves the Lindbladian:

$$\begin{aligned} \mathcal{L}\rho(t) = & -i[H_{\text{TCHM}}, \rho(t)] \\ & + \sum_{n=1}^N \left\{ \frac{\kappa_n}{2} \mathcal{D}[a_n] \rho(t) + \sum_{m=1}^M \frac{\gamma_{n,m}}{2} \mathcal{D}[\sigma_{n,m}^-] \rho(t) \right\} \\ & + P \mathcal{D}[a_1^\dagger] \rho(t) \end{aligned} \quad (3)$$

where $\mathcal{D}[c] \rho(t) = 2c\rho(t)c^\dagger - c^\dagger c\rho(t) - \rho(t)c^\dagger c$, $\kappa_n = \kappa$ is the cavity linewidth of the n -th cavity, $\gamma_{n,m} = \gamma$ is the emission rate of the m -th emitter in the n -th cavity, and P is the optical (laser) pumping term. The spectral intensity reported in Figure 2a is calculated as the Fourier Transform of the correlation function $\langle A^\dagger(t + \tau)A(t) \rangle$:

$$S(\omega) = \int_{-\infty}^{\infty} \lim_{t \rightarrow \infty} \langle A^\dagger(t + \tau)A(t) \rangle e^{-i\omega\tau} d\tau, \quad (4)$$

where A is replaced by the cavity annihilation and the emitter lowering operators, a_n and $\sigma_{n,m}^-$.

The results of the solved QME are shown in Figure 2a for a range of disorders; $\Delta = \epsilon \approx 0$ is the resonant case, $\Delta = \frac{g}{4}\sqrt{M}$ the moderate disorder case, and $\Delta = g\sqrt{M}$ the strongly disordered case. For convenience, we are reporting the sum of the results when the pump term is interacting with Cavity 1 ($P \mathcal{D}[a_1^\dagger] \rho(t)$) and when the pump term is interacting with Cavity 2 ($P \mathcal{D}[a_2^\dagger] \rho(t)$). The complete and unsummed results are available in the Appendix. In these simulations we can draw conclusions about the polaritonic properties of each cavity. For example, in the resonant case, we see a high degree of light-matter interaction based on the relative peak heights of the cavities' spectra vs. the combined peak heights of the corresponding emitters. In a purely resonant case, we would not see the middle subradiant peaks, but to avoid errors from a multiply degenerate zero energy state in our subradiant states, we make $\epsilon \ll 1$ which generates small subradiant peaks. As we move to moderate disorder, the subradiant states grow and then at strong disorder they become the dominant features in the spectrum. These subradiant states are entirely emitter-like which means that the polaritonic properties seen in the resonant case begin breaking down with more disorder.

The QME requires the use of the full density operator because of the non-number conserving term $\rho(t)c^\dagger c$. This density operator requirement makes solving this system highly resource-intensive (the Hilbert space is exponential in $N \times M$) and not sparse, as such we were restricted in our exact calculations to small systems of six elements, or two coupled cavities with two emitters per cavity.

2. The Effective Hamiltonian Approach

To access modeling of larger systems we develop a software package in Python [47] that diagonalizes the Effective Hamiltonian in the approximate single-excitation regime

$$H_{\text{EFF}} = H_{\text{TCHM}} - \frac{i}{2} \sum_{n=1}^N \left\{ \kappa_n a_n^\dagger a_n + \sum_{m=1}^{M_n} \gamma_{n,m} \sigma_{n,m}^+ \sigma_{n,m}^- \right\}, \quad (5)$$

thus reducing the computational complexity from exponential to polynomial (cubic) in $N \times M$ for the single-excitation regime. With this approximate method we numerically solve systems with hundreds of elements compared to the several using the exact QME approach. Note that, in contrast to QME, this method does not contain a pump term, meaning it is agnostic to the starting cavity and its diagonalization will provide all possible states, regardless of their wavelength overlap with the initial cavity.

For the purposes of comparison, the lowest energy eigenstates results for a system with the same parameters as the reported QME results are shown in Figure 2b. These values are obtained by applying each element's number operator to the resulting wavefunctions. We can now determine the polaritonic character of the system by comparing the cavity involvement (blue) to the emitter involvement (red). We again see that as the disorder increases the emitter terms become larger, which is due to the subradiant states playing more of a role in the system. Interestingly, the asymmetry between Cavity 1 and its emitters (Node 1) and Cavity 2 and its emitters (Node 2) becomes more obvious. If we look at the lower energy peak in the the QME, which corresponds well to the lowest energy eigenstate, we can see that for moderate disorder the lines corresponding to Node 1 (Cavity 1, Emitter 1,1, and Emitter 1,2) are shifted to slightly higher energies and are slightly smaller in amplitude. The opposite then occurs for strong disorder with the low energy peaks of Node 2 being shifted up in energy and the amplitudes slightly smaller. This is reproduced in the H_{EFF} approach with the amplitudes of Node 1 (Node 2) being significantly smaller in the moderately (strongly) disordered simulations.

The details of the QME simulations are reproduced down to the relative amplitudes of the emitters within the node. For example in the QME simulations the lower energy peak of Emitter 2,1 has a greater amplitude than that of Emitter 2,2 in the $\Delta = \frac{g}{4}\sqrt{M}$ simulation, which corresponds to the ratios of Emitter 2,1 (dark red) and Emitter 2,2 (light red) in the H_{EFF} simulations. We find this level agreement between the approaches to be enough to confidently scale up to more relevant Hilbert space dimensions using the H_{EFF} approach.

3. The Participation Ratio Approach: Metrics for characterizing disorder

The node-by-node and element-by-element analysis performed in the previous sections is lengthy and not suitable for the much larger systems we will be exploring with the H_{EFF} approach. In order to efficiently analyze these much larger systems, we develop new metrics for the characterization of TCHM wavefunctions, inspired by practices in Condensed Matter Physics. The phenomenon of Anderson localization describes the loss of mobility of quantum particles due to randomness [48]. Originally studied in the context of non-interacting electrons hopping on a lattice with disordered site-energies, where all eigenstates were shown to be localized in spatial dimension less than or equal to two [49, 50], Anderson localization has subsequently been extensively investigated in many further contexts, including the effect of interactions [51], correlations in the disorder [52], and importantly, new experimental realizations from cold atomic gases [53, 54] to transport in photonic lattices [55].

A useful metric for quantifying the localization of a wavefunction v_p , employed in these studies, is the participation ratio, $P = \left[\sum_p |v_p|^4 \right]^{-1}$ [56] and its generalizations [57]. Instead of measuring the participation ratio among all $N(M+1)$ vector components, we adapt P to two new metrics that measure the participation among N nodes (cavity-emitter sets), and two cavity- and emitter-like components. We define the nodal participation ratio,

$$P_N = \left[\sum_{n=1}^N \left(\langle \mathcal{N}_{ph,n} \rangle + \langle \mathcal{N}_{e,n} \rangle \right)^2 \right]^{-1}, \quad (6)$$

where $\mathcal{N}_{ph,n} = a_n^\dagger a_n$ and $\mathcal{N}_{e,n} = \sum_{m=1}^{M_n} \sigma_{n,m}^+ \sigma_{n,m}^-$ are the usual number operators for each state v_p representing cavity excitation and the sum of all emitter excitation in a cavity. Like the classic participation ratio, P_N is at a minimum (maximum) when the wavefunction is localized (delocalized). Next, we define the polaritonic participation ratio, or *polaritonality*,

$$P_P = \left[\left(\sum_{n=1}^N \langle \mathcal{N}_{ph,n} \rangle \right)^2 + \left(\sum_{n=1}^N \langle \mathcal{N}_{e,n} \rangle \right)^2 \right]^{-1}, \quad (7)$$

which is minimized when the wavefunction has completely cavity-like or completely emitter-like character and is maximized for an equal superposition of cavity- and emitter-like components. Note: a wavefunction can be polaritonic even when the cavity and emitter excitations do not belong to the same node.

These two new metrics allow us to seamlessly characterize multi-emitter CCAs. We normalize the metrics to 1 for easy comparison between the different model parameter cases. We apply these metrics to small systems to verify them against the exact solutions before we employ them in larger simulations. For a vanishing disorder

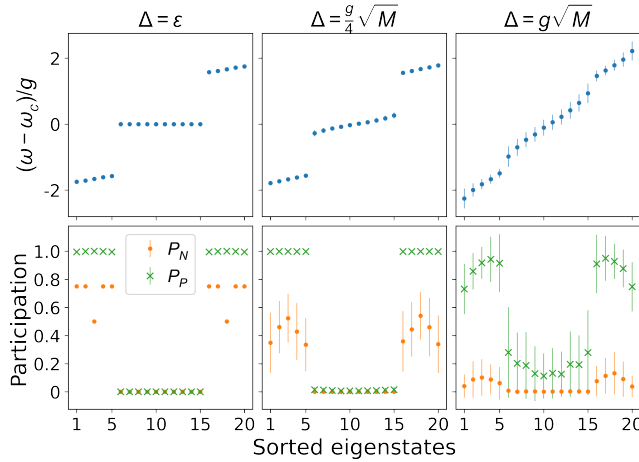


FIG. 3. Effects of increasing disorder, Δ , on the eigenstates of a system of $N = 5$ cavities and $M = 3$ emitters per cavity with $J/g = 0.1$. (Top) Energy eigenvalues and (bottom) participation ratios P_N , P_P . Increasing Δ lifts the degeneracy of the subradiant states (flat middle band) decreasing the gap between the polaritonic bands and the subradiant states. Increasing Δ also causes an Anderson-like node localization in the polariton bands as shown by P_N decreasing, but the polaritonic states remain mostly polaritonic. Mean of 100 random realizations; error bars are one standard deviation. g , κ , γ are same as those in Figure 2a.

($\Delta = \epsilon$, the leftmost column), the probabilities of excitation of Cavity 1 or 2 are $\frac{1}{4}$ each, and the probabilities of excitation of any of the four emitters are $\frac{1}{8}$ each, as shown in the top row. The wave function is maximally spread out both amongst the nodes and also maximally spread between cavities and emitters. The former fact implies P_N should be maximized, and the latter that P_P should be maximized, as is shown in Figure 2c. [58]

We observe the same trends in P_N and P_P as we do in Figures 2a,c; namely, the increase in nodal localization and polaritonicity for increasing disorder. More detailed plots of the three approaches for a range of g/J values can be found in Figure 4 and Section IV. In particular, it is shown that increasing J leads the eigenvector of lowest eigenenergy to become predominantly localized in the cavities. Thus the polaritonic participation P_P falls dramatically, unlike its relative insensitivity to Δ in Fig. 2c. In the following sections we use only the participation ratio approach to look at these much larger systems that may be of interest to future condensed matter quantum simulations.

C. Polaritonicity and localization in medium size TCHM systems

We first investigate the effects of spectral disorder on medium size systems with an open array of $N = 5$ cavities with $M = 3$ emitters per cavity on the localization and polaritonicity of the eigenstates of Eq. 5. Figure 3 again

explores the regime where cavity QED dominates the photon hopping $J/g = 0.1$. For vanishing spectral disorder, the eigenspectrum has the shape resembling the features of Figure 1: two highly polaritonic delocalized CCA bands with $N = 5$ states and $N(M-1) = 10$ highly localized subradiant states, suitably characterized by the polaritonic and nodal participation ratio values. For moderate disorder, the polaritonic properties of eigenstates are maintained, while the nodal delocalization somewhat decreases for polaritonic band states. The degeneracy of the subradiant states is lifted and the spectral gaps diminish with strong disorder, which is usually considered a cutoff for cavity protection. Most states become highly localized and the subradiant states gain a cavity component, as quantified by the increase of the P_P value. Regimes with an increasing rate of photon hopping to cavity QED interaction are detailed in the Appendix. While similar trends can be observed, the main difference is seen in the reduction of the number of polaritonic states in the CCA bands as the wavefunction obtains a higher cavity-like character.

This brings us to look into the formation of a polaritonic state in spectrally disordered CCA QED as a function of an increasing J/g ratio. Figure 4 shows the polaritonicity and localization of the lowest energy eigenstate for an increasing J/g ratio.

When the photonic nature of the interaction increases, so does the cavity-like character of the wavefunction, reducing its level of polaritonicity. While this holds true for low and moderate values of disorder, in the case of high disorder, we observe an increase of P_P , before the decline. This is an artifact of the disorder which randomly modifies the nature of the lowest eigenstate in the system, until the interaction value increases to a level that offsets the issue. This trend is paired with the increase in the delocalization metric P_N as the wavefunction loses the dominant emitter-like characteristic.

However, not all states lose polaritonicity with an increase in the photon hopping rate. Even in the case of large J/g ratio (see Figures A5 and A6 for results for larger J/g values), there still exist highly polaritonic states located in the middle of the lower polariton band

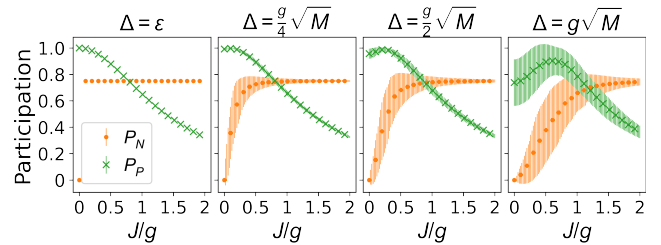


FIG. 4. The nodal and the polaritonic participation ratios for the lowest energy eigenstate of a CCA with $N = 5$ and $M = 3$ for increasing J/g . A small amount of disorder causes the state to node localize for small J/g . Mean of 100 random realizations; error bars are one standard deviation. $N = 5$, $M = 3$; g , κ , γ same as those in Figure 2a.

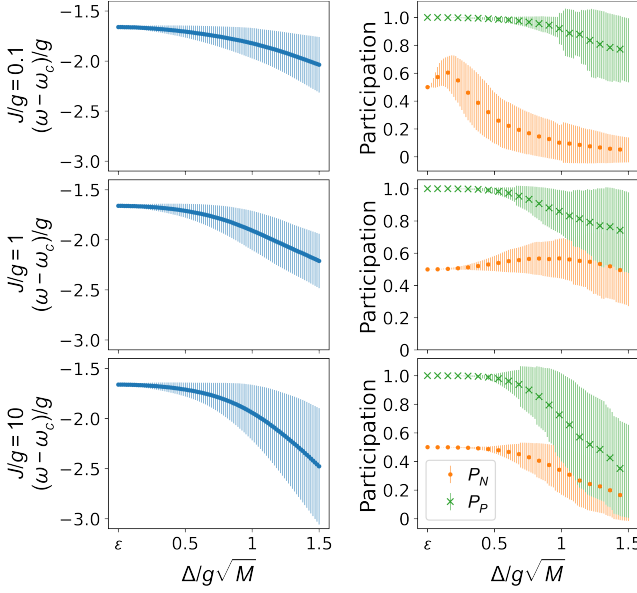


FIG. 5. Changes in the energy and participation metrics as the spectral disorder, Δ , is increased for the most polaritonic state (MPS) of the lower polariton band. Mean of 100 random realizations; error bars are one standard deviation. Participation metrics are normalized to $[0, 1]$. $N = 5$, $M = 3$; g , κ , γ same as those in Figure 2a.

(and an analogous one in the higher polariton band). We refer to these as the most polaritonic states (MPS). As seen in Eqs. A4 and A5 of the Appendix, where we discuss the PAM eigenvectors, the MPS is parameterized by the momentum value $k = \frac{\pi}{2}$ where the cavity and emitter bands cross for $\omega_c = \omega_e$ and hence are maximally mixed. For systems with an odd number of cavities, this state occupies every other node characterized by $P_N \approx 0.5$. Figure 5 shows how this state changes with increasing disorder.

A decrease in polaritonicity and delocalization of the wavefunction take place for a range of system parameters. We note that for the case of $J/g = 1$ the wavefunction has a delayed localization trend. At low J/g there is less variance in P_P for a larger Δ compared to a higher photon hopping rate, suggesting that, as in the single node Tavis-Cummings model [27], the stronger cavity-emitter coupling compared to combined cavity losses (in the TCHM this includes cavity-cavity coupling) provides better cavity protection against the disorder in the TCHM.

D. Cavity protection in large TCHM systems

Next, we look at how the system size (N, M) under open boundary condition affects localization and cavity protection by studying P_N and P_P trends for the MPS of the lower polariton band. To quantify the cavity protection effect, we here define the cavity protection regime as $P_P \geq 0.8$ for the MPS and normalized P_P .

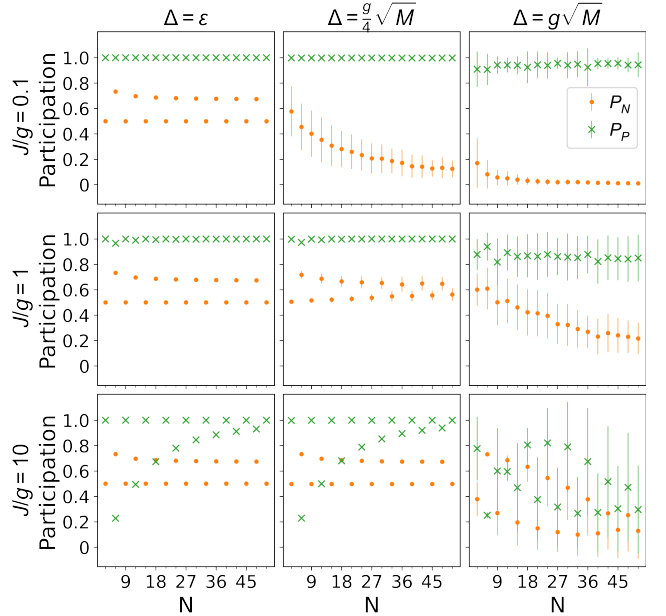


FIG. 6. Participation metrics for the most polaritonic state (MPS) of the lower polariton band for an increasing N . There are two distinct bands for each metric due to the parity of N which converge at its large values. Mean of 100 random realizations; error bars are one standard deviation. $M = 3$; g , κ , γ same as those in Figure 2a.

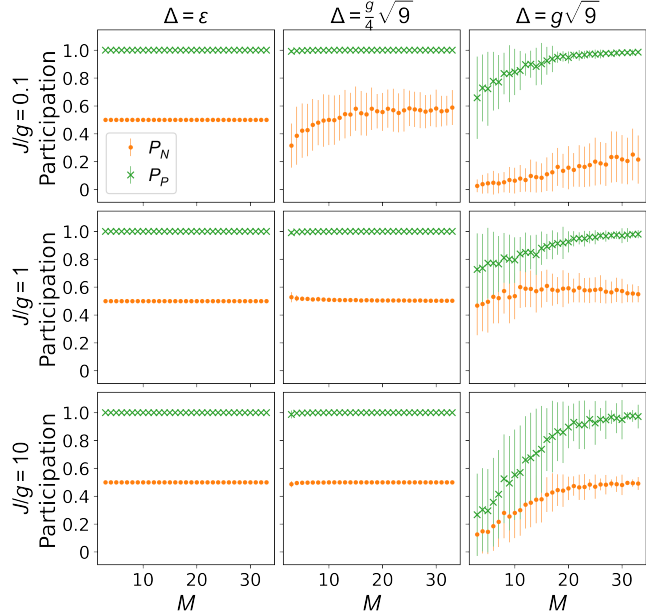


FIG. 7. Nodal and polaritonic participation ratios as a function of number of emitters M for the MPS. Increasing the number of emitters increases the cavity protection against the spectral disorder of emitter ensemble without causing node localization. Cavity protection is achieved when $P_P \geq 0.8$ for the MPS, which occurs when there are at least M emitters per cavity for spectral disorder of $\Delta = g\sqrt{M}$ for $J/g \leq 1$. Mean of 100 random realizations; error bars are one standard deviation. $N = 5$, $M_{min} = 3$; g , κ , γ same as those in Figure 2a.

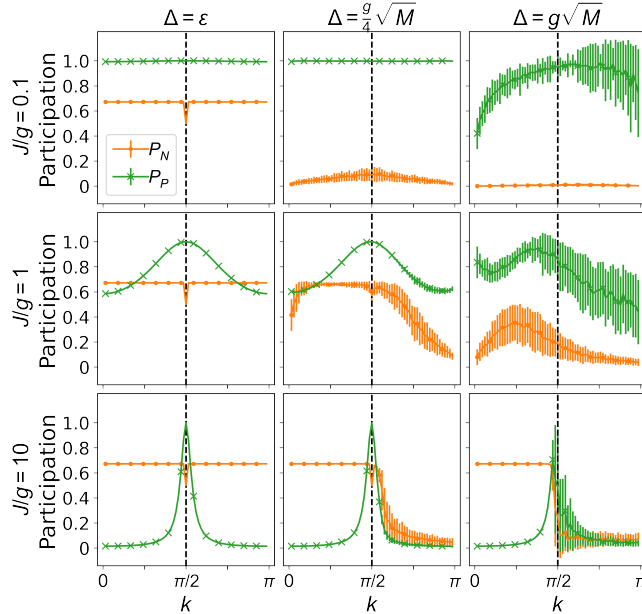


FIG. 8. Participation ratios with an increasing disorder, Δ , of the lower polariton band of eigenstates for CCA with $N = 65$, $M = 3$. Vertical dashed line is $k = \frac{\pi}{2}$. Mean of 100 random realizations; error bars are standard deviation. g , κ , γ same as those in Figure 2a.

We observe that the parity of the number of cavities plays a role in the properties of the MPS. For an increasing N , shown in Figure 6, two distinct bands emerge for each metric, but converge for large N . This occurs because only odd N has an eigenstate at exactly $k = \frac{\pi}{2}$. We also observe that for nonvanishing disorder, longer CCAs localize the MPS, especially for the low J/g ratio. Another way to describe this dependence on CCA size is that there is a finite localization length ξ , and with increasing $N \gtrsim \xi$, it becomes more evident that the MPS occupies only a fraction of the whole array.

The number of emitters per cavity appears to have a strong influence on the formation of polaritons, as in the Tavis-Cummings model. Increasing the number of emitters M , as shown in Figure 7, effectively increases the cavity-emitter coupling $g \rightarrow g\sqrt{M}$, thus improving the polaritonic nature of the eigenstate and delocalization against disorder. For constant Δ , we increase M to estimate the number of emitters required to reach the cavity protection regime. Consistent with the prior studies of cavity protection, we find that at low hopping rates, $J/g \leq 1$, to reach $P_P \geq 0.8$ for $\Delta = g\sqrt{M}$ we need approximately M emitters per cavity.

The Effective Hamiltonian approach and the two participation ratio metrics equip us to explore larger CCA QED systems. Studying the lower polariton band of larger systems with $N = 65$ cavities and $M = 3$ emitters per cavity, as shown in Figure 8, it is easy to visualize the effects of disorder on localization and polariton formation. We see that disorder of the emitter fre-

quencies causes an Anderson-like localization in the nodes reflected in the reduction of the P_N metrics. This localization occurs first in the emitter-like eigenstates, the states with $k > \frac{\pi}{2}$, and then the cavity-like states become more localized with an increasing disorder Δ . Additionally, among the emitter-like eigenstates, the variance in P_P increases with a growing Δ . For small J/g ratios, the states at $k \leq \frac{\pi}{2}$ become dominantly emitter-like with an increasing disorder and lose their polaritonicity. The P_P values become more defined with an increasing J/g ratio.

IV. DISCUSSION

In this work we characterize the CCA QED eigenstates described by the Tavis-Cummings-Hubbard model. Our goal is to provide a guiding tool for experimental implementations through the engineering of the CCA parameters.

Using the new participation ratio metrics, inspired by condensed matter physics studies of localization and band mixing, we confirm that highly polaritonic states can be formed in coupled cavity arrays despite the presence of spectral disorder in emitter ensembles and quantify the cavity protection effect. While the systems with a dominant cavity QED interaction, relative to the photon hopping rate, support creation of numerous polaritonic states, we find that other parts of the parameter space can also be utilized to study polaritonic physics.

We suggested approximate analogies between the case of $M_n = 1$ emitter in each cavity with the periodic Anderson model where a single f orbital on each site hybridizes with a conduction band, and the Kondo lattice model where the local degree of freedom is spin-1/2. Condensed matter systems which connect to the multi-emitter case $M_n > 1$ also have a long history, both in the investigation of multi-band materials and also as a theoretical tool providing an analytically tractable *large-N* limit [59, 60]. Indeed, large- N systems, realized for example by alkaline earth atoms in optical lattices, are also at the forefront of recent work in the atomic, molecular and optical physics community [61–63]. In short, the TCHM offers a context to explore intertwined local and itinerant quantum degrees of freedom which, while distinct from condensed matter models, might still offer insight into their behavior.

These TCHM systems can ostensibly be realized in a number of photonic frameworks, from atoms in mirrored cavities, to quantum dots in nanophotonics. It is difficult, however, to experimentally create atom-based systems that couple multiple cavities together and to create large numbers of quantum dots that emit within the relatively modest range of disorder that we have shown will recreate polariton dynamics. As such, the most likely experimental realization of our systems will be in color center based nanophotonics.

Acknowledgements M.R. and V.A.N. acknowledge

support by the National Science Foundation CAREER award 2047564. R.T.S. was supported by the grant DE-SC0014671 funded by the U.S. Department of Energy, Office of Science.

Appendix A: Condensed Matter analogies

The resonant cavity-emitter arrays ($\omega_{c,n} = \omega_c$, $\omega_{e,n,m} = \omega_e$, $g_{n,m} = g$, $J_{n,n+1} = J$), with periodic boundary conditions have a closed form solution for the eigenvalues and eigenvectors. Much of the derivation precisely parallels the calculation of the band structure of tight binding Hamiltonians. The case of no emitters ($M_n = 0$) corresponds to the $d = 1$ (Bose) Hubbard Model (HM), and the case with a single emitter in each cavity ($M_n = 1$) to the Periodic Anderson Model (PAM). Here we review those results with an emphasis on the condensed matter analogies.

In the case $M_n = 0$ one can diagonalize H_{TCHM} by introducing momentum creation and destruction operators,

$$a_k^\dagger = \frac{1}{\sqrt{N}} \sum_{l=1}^N e^{ikl} a_l^\dagger \quad a_k = \frac{1}{\sqrt{N}} \sum_{l=1}^N e^{-ikl} a_l \quad (\text{A1})$$

The transformation is canonical. a_k^\dagger and a_k obey the same bosonic commutation relations as the original real space operators. H_{TCHM} is diagonal,

$$H_{\text{TCHM}} = \sum_k (\omega_c - 2J \cos k) a_k^\dagger a_k \quad (\text{A2})$$

The eigenenergies are,

$$E(k) = \omega_c - 2J \cos k. \quad (\text{A3})$$

The momenta are discrete, $k = k_p = 2\pi p/N$ with $p = 1, 2, 3, \dots, N$. In the thermodynamic limit the $E(k)$ form a continuous band with a density of states that diverges at the band edges $E(k) = \omega_c \pm 2J$.

In this no-emitter limit, Eq. A2 actually provides the solution for any number of excitations. The many-excitation energies are just sums of the single particle $E(k)$ subject to the photon indistinguishability implied by the commutation relations. This solubility of the many excitation system is unique to the no-emitter limit, as discussed further below.

In the case $M_n = M = 1$ one can again solve for the eigenvalues of H_{TCHM} by going to momentum space, but only in the single excitation sector. The reason is that the photon and emitter operators do not obey a consistent set of commutation relations. Thus, even though it might appear that H_{TCHM} is soluble since it is quadratic in the operators, it is therefore not possible to do the same sort of canonical transformation to diagonalize. It is most straightforward to define a set of single excitation states which form a basis for the space, and then examine

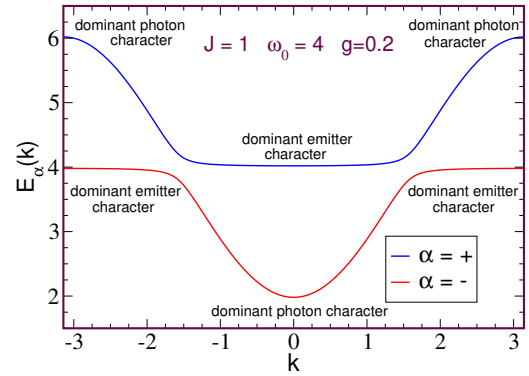


FIG. A1. The two polariton bands of a cavity-emitter system for representative parameters $\omega_c = \omega_e \equiv \omega_0 = 4$, cavity hopping $J = 1$, and cavity-emitter coupling $g = 0.2$. If the number of emitters $M > 1$ the gap between the two bands is enhanced from $\Delta = 2g$ to $\Delta = 2\sqrt{M}g$ and there are $M-1$ additional flat emitter bands at $E_\alpha(k) = \omega_0$ in the gap between the two polariton bands.

the matrix which arises from the application of H_{TCHM} to each one. For simplicity, we focus on the *resonant* case where $\omega_c = \omega_e \equiv \omega_0$, but the formulae are straightforward to generalize. The energy eigenvalues are

$$E(k) = \omega_0 - J \cos k \pm \sqrt{J^2 \cos^2 k + g^2}. \quad (\text{A4})$$

The (unnormalized) eigenvectors are,

$$\Psi_\pm(k) = \begin{pmatrix} g \\ J \cos k \mp \sqrt{J^2 \cos^2 k + g^2} \end{pmatrix} \quad (\text{A5})$$

so that, while all states are polaritons in the sense of mixing photon and emitter components, the relative weights depend on momentum k and band index \pm .

This $M_n = M = 1$ case easily generalizes to larger M . There are again two polariton bands, but with an enhanced photon-emitter hybridization $\sqrt{M}g$,

$$E(k) = \omega_0 - J \cos k \pm \sqrt{J^2 \cos^2 k + Mg^2}. \quad (\text{A6})$$

with a similar $g^2 \rightarrow Mg^2$ change to the eigenvectors of Eq. A5. The remaining $M-1$ bands have purely emitter components, and are dispersionless, $E(k) = \omega_0$.

A useful approximate visualization of the eigenvalues and eigenvector weights is provided by drawing the bands as in Figure A1. For $g = 0$ the photons have $E(k) = \omega_0 - 2J \cos k$ and the emitters $E(k) = \omega_0$. When these two energy levels are hybridized by g there is a level repulsion at their crossing point at $k = \pm\frac{\pi}{2}$ and an energy gap $\Delta = 2g$ opens. The relative photon-emitter compositions of the states can be inferred from the degree to which the polariton energy matches one of the initial ($g = 0$) photon or emitter bands. Polariton energies which are close to the original flat $E(k) = \omega_0$ emitter band are

dominantly made up of emitter excitations, while those close to the original dispersing $\omega_0 - 2J \cos k$ photon band are dominantly cavity excitations.

Appendix B: Exact simulation results

We numerically solve the quantum master equation for a coupled 2 cavity system with each cavity also coupling to two emitters each. The results are shown in Figure A2. Along the top row, which shows the smallest inter-cavity coupling simulations, we see the most nodal localization regardless of emitter dispersion, as shown by only having peaks in Cavity 1 and Emitters 1 and 2 when pumping Cavity 1 and only having peaks in Cavity 2 and Emitters 3 and 4 when pumping Cavity 2. We can also see that the small inter-cavity coupling leads to highly polaritonic systems by comparing the peak heights of each cavity to those of its emitters and finding the ratios are close to unity (0.78 - 0.9). The largest inter-cavity coupling, $J/g = 10$ is heavily cavity-like as shown by cavity peak to emitter peak ratios of around 50. The middle row, $J/g = 1$ is partially polaritonic and partially photonic with peak ratios in the range 0.3-0.6. By introducing nonzero emitter detuning, we are able to access subradiant states for each of the three detuning values. These states are identified by the zero-width peaks found between the polariton peaks. Subradiant states are states that decay much slower than the polariton peaks and a number of proposals exist for their use in quantum information technologies including, light storage [64] and quantum light generation [29].

Appendix C: Benchmarking of the Effective Hamiltonian approximation and the participation ratio metrics

To benchmark the approximate Effective Hamiltonian approach against the exact Quantum Master Equation solution, we simulate the systems with same parameters in both models. The Figure A3 shows the lowest energy wavefunction calculated with the Effective Hamiltonian approach, corresponding to the excitations of the lowest energy peaks in the Figure A2. The case of the vanishing spectral disorder shows equal contribution of Cavity 1 and 2, which corresponds to the identical looking plots of the Cavity 1 and Cavity 2 excitations in the QME spectra when Cavity 1 and Cavity 2 are pumped, respectively. The asymmetry of the nodal occupations in Figure A3 for non-vanishing disorder (especially for $J/g = 0.1$) matches the non-identicality of the Cavity 1/2, as well as Emitter 1.1,1.2 and Emitter 2.1,2.2 spectra in Figure A2. Localization of the wavefunction for an increasing disorder and $J/g \leq 1$ follow the exact solution trends described in the previous section.

These parallels are closely described by the nodal P_N and the polaritonic P_P participation ratio shown in Fig-

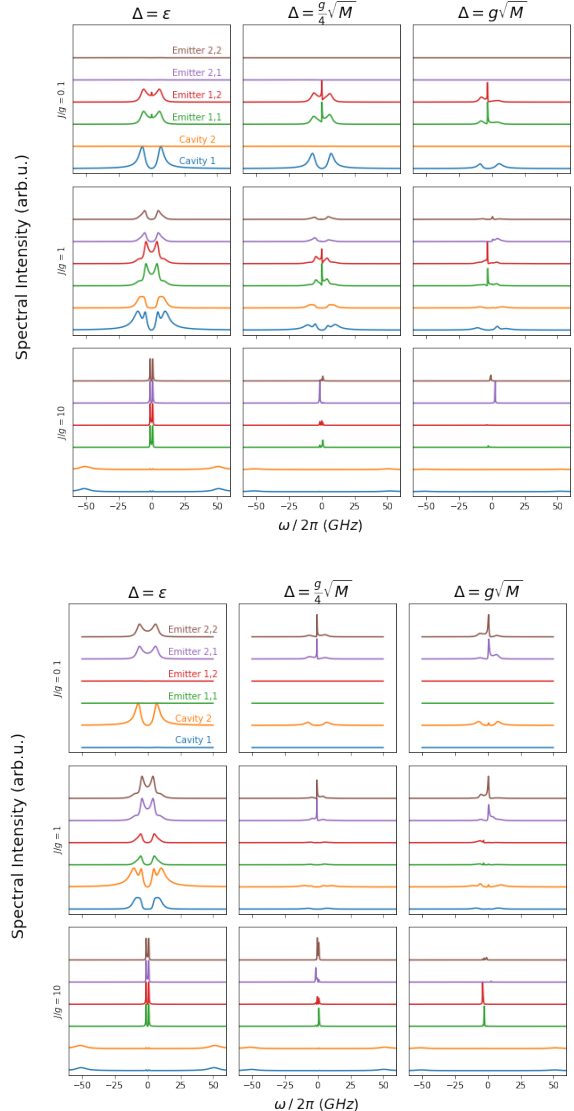


FIG. A2. The top plots show the pump operator acting on Cavity 1 and the bottom set show the pump term acting on Cavity 2. Each line within a subplot refers to the transmission spectrum acquired by probing a particular element of the systems, either Cavities or any of the Emitters. Cavity 1 (blue) is coupled to Emitters 1,1 and 1,2 (green and red respectively). Cavity 2 is coupled to Emitters 2,1 and 2,2 (purple and brown respectively). The rows correspond to different cavity-cavity coupling ratios, with $J/g = 0.1$ (top row) having the least coupling between cavities, and $J/g = 10$ (bottom row) having the most. Moving from left to right increases the amount of disorder introduced via emitter emission wavelength detuning from a nominally zero amount (ϵ), to detuning approximately equal to the cavity-emitter coupling (g).

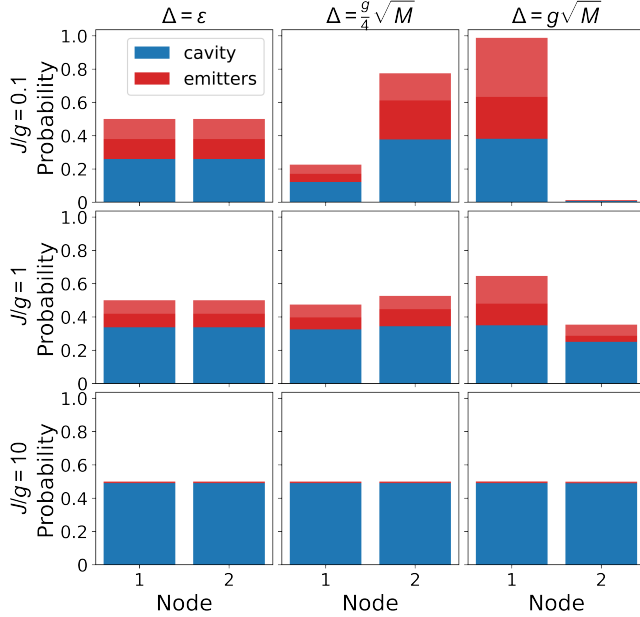


FIG. A3. Node occupancy of the lowest energy eigenstate of a system with $N = 2$ cavities and $M = 2$ emitters per cavity with random ω_e sampled from a Gaussian distribution of width Δ . Single random realization for each Δ . g , κ , γ , and emitter frequencies are the same as those in Figure A2.

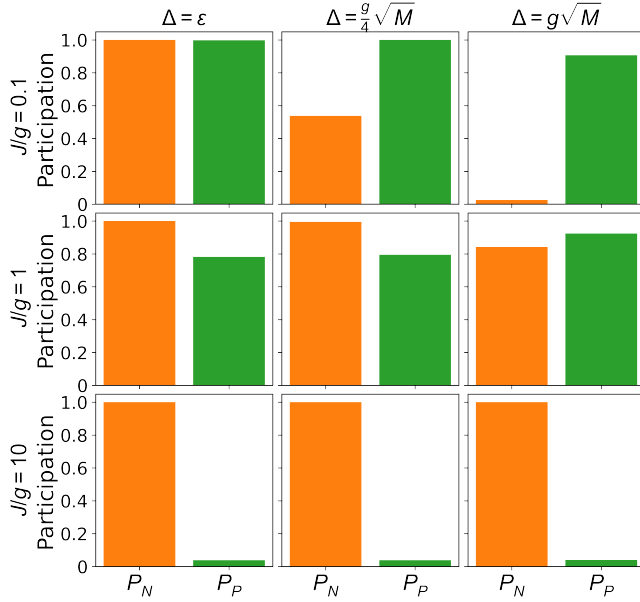


FIG. A4. Participation ratios of the lowest energy eigenstate for a system with $N = 2$ cavities and $M = 2$ emitters per cavity with random ω_e sampled from a Gaussian distribution of width Δ . Single random realization for each Δ . $g = 5$, $\kappa = 10$, $\gamma = 1/5.8$. The emitter frequencies are the same as those in Figure A2.

ure A4. The value of P_N (orange) is maximized for a fully node-delocalized wavefunction, and reduces as the wavefunction tends to increasingly excite one cavity and its emitters with an increasing disorder. The value of P_P (green) is maximized for the wavefunctions that have equal excitation distribution between cavities and the emitters, and reduces with an increasing photonic interaction (high J/g value) as the cavities become predominantly excited.

We conclude that the Effective Hamiltonian and the participation ratio metrics are suitable for studies of the Tavis-Cummings-Hubbard model.

Appendix D: Effects of spectral disorder on the TCHM energy spectrum

We utilize the Effective Hamiltonian approach to study medium and large TCHM systems and are especially concerned with the influence of the spectral disorder on the polaritonic and localization properties of the model wavefunctions. The Figure A6 shows the energy spectra of an $N = 5, M = 3$ system for various regimes of cavity QED to photon hopping ratios. For the vanishing disorder, we clearly see the three components of the spectrum illustrated in the Figure 1: two polaritonic bands with N states and a subradiant band with $N(M - 1)$ degenerate states. When cavity QED interaction is significant, a band gap opens between the polariton bands and the subradiant states. With an increasing spectral disorder, the band gap closes and the subradiant state degeneracy is lifted.

Further analysis is provided by the corresponding P_N and P_P values shown in Figure A6. Here, we observe that the polaritonic properties of the highly hybridized states in the polariton bands and the emitter-like states in the subradiant band shift significantly only for the high levels of spectral disorder, defined by the typical cavity protection cutoff $\Delta = g\sqrt{M}$. The increasing localization trend (decreasing P_N) for most polariton band states with an increasing disorder is evident for all sets of parameters. In contrast, the subradiant states gain a cavity component with an increasing disorder and become more hybridized and delocalized.

While the polaritonicity of the lower (as well as the upper) polariton band reduces for most states with an increasing J/g ratio, the middle state of the band remains highly polaritonic. This state, labeled the most polaritonic state (MPS) in our study, shows that even the systems with high hopping ratio can serve as testbeds for polaritonic physics explorations.

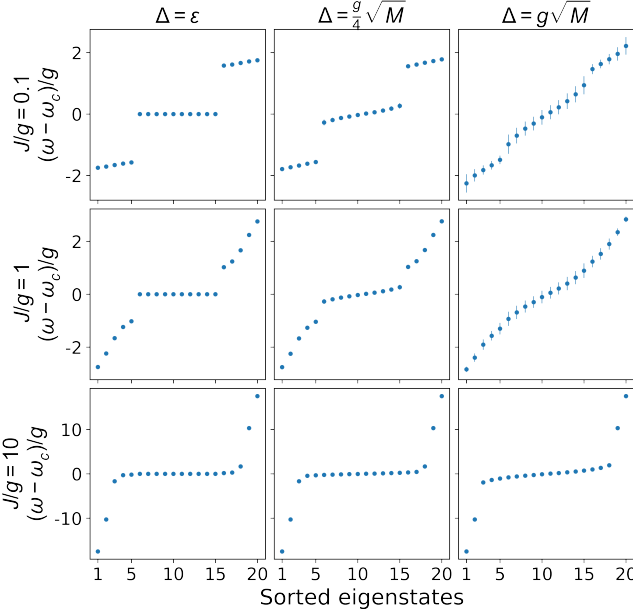


FIG. A5. Effects of an increasing disorder, Δ , on the energy eigenspectrum for 3 different J/g values. Mean of 100 random realizations; error bars are one standard deviation. $N = 5$, $M = 3$; g , κ , γ same as those in Figure A2

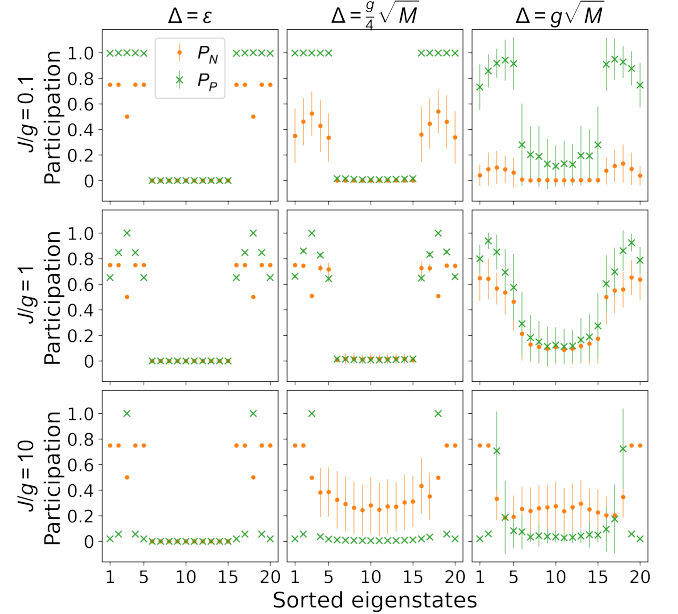


FIG. A6. Effects of an increasing disorder, Δ , on the localization and polaritonality of the eigenstates for 3 different J/g values. For large J/g there remains two polaritonic states located in the middle of the polariton bands. Mean of 100 random realizations; error bars are one standard deviation. $N = 5$, $M = 3$; g , κ , γ same as those in Figure A2

[1] R. P. Feynman, Simulating physics with computers, in *Feynman and computation* (CRC Press, 2018) pp. 133–153.

[2] E. Altman, K. R. Brown, G. Carleo, L. D. Carr, E. Demler, C. Chin, B. DeMarco, S. E. Economou, M. A. Eriks-
son, K.-M. C. Fu, *et al.*, Quantum simulators: Architectures and opportunities, *Physical Review X Quantum* **2**, 017003 (2021).

[3] I. M. Georgescu, S. Ashhab, and F. Nori, Quantum simulation, *Reviews of Modern Physics* **86**, 153 (2014).

[4] J. I. Cirac and P. Zoller, Goals and opportunities in quantum simulation, *Nature Physics* **8**, 264 (2012).

[5] A. Trabesinger, Quantum simulation, *Nature Physics* **8**, 263 (2012).

[6] S. Schmidt and J. Koch, Circuit QED lattices: Towards quantum simulation with superconducting circuits, *Annales der Physik* **525**, 395 (2013).

[7] C. Noh and D. G. Angelakis, Quantum simulations and many-body physics with light, *Reports on Progress in Physics* **80**, 016401 (2016).

[8] A. Saxena, Y. Chen, Z. Fang, and A. Majumdar, Photonic topological baths for quantum simulation, *arXiv preprint arXiv:2106.14325* (2021).

[9] A. Aspuru-Guzik and P. Walther, Photonic quantum simulators, *Nature Physics* **8**, 285 (2012).

[10] X.-W. Luo, X. Zhou, C.-F. Li, J.-S. Xu, G.-C. Guo, and Z.-W. Zhou, Quantum simulation of 2D topological physics in a 1D array of optical cavities, *Nature Communications* **6**, 1 (2015).

[11] M. J. Hartmann, F. G. Brandao, and M. B. Plenio, Quantum many-body phenomena in coupled cavity arrays, *Laser & Photonics Reviews* **2**, 527 (2008).

[12] J. Vučković, D. Fattal, C. Santori, G. S. Solomon, and Y. Yamamoto, Enhanced single-photon emission from a quantum dot in a micropost microcavity, *Applied Physics Letters* **82**, 3596 (2003).

[13] J. P. Reithmaier, G. Sek, A. Löffler, C. Hofmann, S. Kuhn, S. Reitzenstein, L. Keldysh, V. Kulakovskii, T. Reinecke, and A. Forchel, Strong coupling in a single quantum dot–semiconductor microcavity system, *Nature* **432**, 197 (2004).

[14] A. Faraon, I. Fushman, D. Englund, N. Stoltz, P. Petroff, and J. Vučković, Coherent generation of non-classical light on a chip via photon-induced tunnelling and blockade, *Nature Physics* **4**, 859 (2008).

[15] G. Shambat, B. Ellis, A. Majumdar, J. Petykiewicz, M. A. Mayer, T. Sarmiento, J. Harris, E. E. Haller, and J. Vučković, Ultrafast direct modulation of a single-mode photonic crystal nanocavity light-emitting diode, *Nature Communications* **2**, 1 (2011).

[16] G. M. Almeida, F. Ciccarello, T. J. Apollaro, and A. M. Souza, Quantum-state transfer in staggered coupled-cavity arrays, *Physical Review A* **93**, 032310 (2016).

[17] S. Bose, D. G. Angelakis, and D. Burgarth, Transfer of a polaritonic qubit through a coupled cavity array, *Journal of Modern Optics* **54**, 2307 (2007).

[18] S. Schmidt and G. Blatter, Strong coupling theory for the Jaynes-Cummings-Hubbard model, *Physical Review*

Letters **103**, 086403 (2009).

[19] A. L. Hayward, A. M. Martin, and A. D. Greentree, Fractional quantum Hall physics in Jaynes-Cummings-Hubbard lattices, *Physical Review Letters* **108**, 223602 (2012).

[20] A. Majumdar, A. Rundquist, M. Bajcsy, and J. Vučković, Cavity quantum electrodynamics with a single quantum dot coupled to a photonic molecule, *Physical Review B* **86**, 045315 (2012).

[21] A. Majumdar, A. Rundquist, M. Bajcsy, V. D. Dasika, S. R. Bank, and J. Vučković, Design and analysis of photonic crystal coupled cavity arrays for quantum simulation, *Physical Review B* **86**, 195312 (2012).

[22] A. Sipahigil, R. E. Evans, D. D. Sukachev, M. J. Burek, J. Borregaard, M. K. Bhaskar, C. T. Nguyen, J. L. Pacheco, H. A. Atikian, C. Meuwly, *et al.*, An integrated diamond nanophotonics platform for quantum-optical networks, *Science* **354**, 847 (2016).

[23] J. L. Zhang, S. Sun, M. J. Burek, C. Dory, Y.-K. Tzeng, K. A. Fischer, Y. Kelaita, K. G. Lagoudakis, M. Radulaski, Z.-X. Shen, *et al.*, Strongly cavity-enhanced spontaneous emission from silicon-vacancy centers in diamond, *Nano letters* **18**, 1360 (2018).

[24] D. M. Lukin, C. Dory, M. A. Gildry, K. Y. Yang, S. D. Mishra, R. Trivedi, M. Radulaski, S. Sun, D. Vercruyse, G. H. Ahn, *et al.*, 4h-silicon-carbide-on-insulator for integrated quantum and nonlinear photonics, *Nature Photonics* **14**, 330 (2020).

[25] D. O. Bracher, X. Zhang, and E. L. Hu, Selective Purcell enhancement of two closely linked zero-phonon transitions of a silicon carbide color center, *Proceedings of the National Academy of Sciences* **114**, 4060 (2017).

[26] M. Lei, R. Fukumori, J. Rochman, B. Zhu, M. Endres, J. Choi, and A. Faraon, Many-body cavity quantum electrodynamics with driven inhomogeneous emitters, *Nature* **10.1038/s41586-023-05884-1** (2023).

[27] M. Radulaski, K. A. Fischer, and J. Vučković, Nonclassical light generation from iii–v and group-iv solid-state cavity quantum systems, in *Advances In Atomic, Molecular, and Optical Physics*, Vol. 66 (Elsevier, 2017) pp. 111–179.

[28] T. Zhong, J. M. Kindem, J. Rochman, and A. Faraon, Interfacing broadband photonic qubits to on-chip cavity-protected rare-earth ensembles, *Nature Communications* **8**, 1 (2017).

[29] M. Radulaski, K. A. Fischer, K. G. Lagoudakis, J. L. Zhang, and J. Vučković, Photon blockade in two-emitter-cavity systems, *Physical Review A* **96**, 011801 (2017).

[30] R. Trivedi, M. Radulaski, K. A. Fischer, S. Fan, and J. Vučković, Photon blockade in weakly driven cavity quantum electrodynamics systems with many emitters, *Physical Review Letters* **122**, 243602 (2019).

[31] A. D. White, R. Trivedi, K. Narayanan, and J. Vučković, Superradiance in dynamically modulated Tavis-Cummings model with spectral disorder, *arXiv preprint arXiv:2108.08397* (2021).

[32] R. Düll, A. Kulagin, W. Lee, Y. Ozhigov, H. Miao, and K. Zheng, Quality of control in the Tavis–Cummings–Hubbard model, *Computational Mathematics and Modeling*, 1 (2021).

[33] B. Sciolla and G. Biroli, Dynamical transitions and quantum quenches in mean-field models, *Journal of Statistical Mechanics: Theory and Experiment* **2011**, P11003 (2011).

[34] R. E. Evans, M. K. Bhaskar, D. D. Sukachev, C. T. Nguyen, A. Sipahigil, M. J. Burek, B. Machielse, G. H. Zhang, A. S. Zibrov, E. Bielejec, *et al.*, Photon-mediated interactions between quantum emitters in a diamond nanocavity, *Science* **362**, 662 (2018).

[35] S. Majety, V. A. Norman, L. Li, M. Bell, P. Saha, and M. Radulaski, Quantum photonics in triangular-cross-section nanodevices in silicon carbide, *Journal of Physics: Photonics* **3**, 034008 (2021).

[36] T. Schröder, M. E. Trusheim, M. Walsh, L. Li, J. Zheng, M. Schukraft, A. Sipahigil, R. E. Evans, D. D. Sukachev, C. T. Nguyen, *et al.*, Scalable focused ion beam creation of nearly lifetime-limited single quantum emitters in diamond nanostructures, *Nature communications* **8**, 1 (2017).

[37] C. Babin, R. Stöhr, N. Morioka, T. Linkewitz, T. Steidl, R. Wörnle, D. Liu, E. Hesselmeier, V. Vorobyov, A. Denisenko, *et al.*, Fabrication and nanophotonic waveguide integration of silicon carbide colour centres with preserved spin-optical coherence, *Nature materials* **21**, 67 (2022).

[38] Z. Shang, A. Hashemi, Y. Berencén, H.-P. Komsa, P. Erhart, S. Zhou, M. Helm, A. Krasheninnikov, and G. Astakhov, Local vibrational modes of Si vacancy spin qubits in SiC, *Physical Review B* **101**, 144109 (2020).

[39] M. E. Bathen, A. Galeckas, R. Karsthof, A. Delteil, V. Sallet, A. Y. Kuznetsov, and L. Vines, Resolving jahn-teller induced vibronic fine structure of silicon vacancy quantum emission in silicon carbide, *Physical Review B* **104**, 045120 (2021).

[40] S. Majety, P. Saha, V. A. Norman, and M. Radulaski, Quantum information processing with integrated silicon carbide photonics, *Journal of Applied Physics* **131**, 130901 (2022).

[41] D. M. Lukin, M. A. Gildry, J. Yang, M. Ghezelou, S. D. Mishra, H. Abe, T. Ohshima, J. Ul-Hassan, and J. Vučković, Optical superradiance of a pair of color centers in an integrated silicon-carbide-on-insulator microresonator, *arXiv preprint arXiv:2202.04845* (2022).

[42] M. E. Trusheim, B. Pingault, N. H. Wan, M. Gündoğan, L. De Santis, R. Debroux, D. Gangloff, C. Purser, K. C. Chen, M. Walsh, *et al.*, Transform-limited photons from a coherent tin-vacancy spin in diamond, *Physical review letters* **124**, 023602 (2020).

[43] D. Manzano, A short introduction to the Lindblad master equation, *AIP Advances* **10**, 025106 (2020).

[44] N. Laflorencie, Quantum entanglement in condensed matter systems, *Physics Reports* **646**, 1 (2016).

[45] V. Norman, Tavis-Cummings-Hubbard open quantum system solver in the quantum master equation approach, <https://github.com/radulaski/Tavis-Cummings-Hubbard-QME> (2021).

[46] J. Johansson, P. Nation, and F. Nori, QuTiP 2: A Python framework for the dynamics of open quantum systems, *Computer Physics Communications* **184**, 1234 (2013).

[47] J. Patton, Tavis-Cummings-Hubbard open quantum system solver in the effective hamiltonian approach, <https://github.com/radulaski/Tavis-Cummings-Hubbard-Heff> (2021).

[48] P. W. Anderson, Absence of diffusion in certain random lattices, *Physical Review* **109**, 1492 (1958).

[49] E. Abrahams, P. Anderson, D. Licciardello, and T. Ramakrishnan, Scaling theory of localization: Absence of quantum diffusion in two dimensions, *Physical Review*

Letters **42**, 673 (1979).

[50] P. A. Lee and T. V. Ramakrishnan, Disordered electronic systems, *Review Modern Physics* **57**, 287 (1985).

[51] E. Miranda and V. Dobrosavljević, Disorder-driven non-Fermi liquid behaviour of correlated electrons, *Reports on Progress in Physics* **68**, 2337 (2005).

[52] A. Croy, P. Cain, and M. Schreiber, Anderson localization in 1D systems with correlated disorder, *The European Physical Journal B* **82**, 107 (2011).

[53] Y. P. Chen, J. Hitchcock, D. Dries, M. Junker, C. Welford, and R. G. Hulet, Phase coherence and superfluid-insulator transition in a disordered Bose-Einstein condensate, *Physical Review A* **77**, 033632 (2008).

[54] M. White, M. Pasienski, D. McKay, S. Q. Zhou, D. Ceperley, and B. DeMarco, Strongly interacting bosons in a disordered optical lattice, *Physical Review Letters* **102**, 055301 (2009).

[55] M. Segev, Y. Silberberg, and D. N. Christodoulides, Anderson localization of light, *Nature Photonics* **7**, 197 (2013).

[56] B. Kramer and A. MacKinnon, Localization: theory and experiment, *Reports on Progress in Physics* **56**, 1469 (1993).

[57] N. C. Murphy, R. Wortis, and W. A. Atkinson, Generalized inverse participation ratio as a possible measure of localization for interacting systems, *Physical Review B* **83**, 184206 (2011).

[58] Since $\langle \mathcal{N}_{ph,1} \rangle = \langle \mathcal{N}_{ph,2} \rangle = \frac{1}{4}$, and $\langle \mathcal{N}_{e,1} \rangle = \langle \mathcal{N}_{e,2} \rangle = \langle \mathcal{N}_{e,3} \rangle = \langle \mathcal{N}_{e,4} \rangle = \frac{1}{8}$, the explicit calculation from Eq. 6 is $P_N = ((\frac{1}{4} + \frac{1}{8} + \frac{1}{8})^2 + (\frac{1}{4} + \frac{1}{8} + \frac{1}{8})^2)^{-1} = 2$. This is the maximal possible value and is then normalized to $P_N = 1$. Likewise from Eq. 7, $P_P = ((\frac{1}{4} + \frac{1}{4})^2 + (\frac{1}{8} + \frac{1}{8} + \frac{1}{8} + \frac{1}{8})^2)^{-1} = 2$.

[59] N. Bickers, D. Cox, and J. Wilkins, Self-consistent large-n expansion for normal-state properties of dilute magnetic alloys, *Physical Review B* **36**, 2036 (1987).

[60] N. Bickers, Review of techniques in the large-N expansion for dilute magnetic alloys, *Reviews of Modern Physics* **59**, 845 (1987).

[61] S. Taie, R. Yamazaki, S. Sugawa, and Y. Takahashi, An SU(6) Mott insulator of an atomic Fermi gas realized by large-spin Pomeranchuk cooling, *Nature Physics* **8**, 825 (2012).

[62] H. Ozawa, S. Taie, Y. Takasu, and Y. Takahashi, Anti-ferromagnetic spin correlation of SU(N) Fermi gas in an optical superlattice, *Physical Review Letters* **121**, 225303 (2018).

[63] E. Ibarra-García-Padilla, S. Dasgupta, H.-T. Wei, S. Taie, Y. Takahashi, R. T. Scalettar, and K. R. Hazard, Universal thermodynamics of an SU(N) Fermi-Hubbard model, *Physical Review A* **104**, 043316 (2021).

[64] G. Facchinetto, S. Jenkins, and J. Ruostekoski, Storing light with subradiant correlations in arrays of atoms., *Physical Review Letters* **117**, 243601 (2016).